

# Holographic Vector Field Electron Tomography of Three-Dimensional Nanomagnets

Daniel Wolf,<sup>1,\*</sup> Nicolas Biziere,<sup>2</sup> Sebastian Sturm,<sup>1</sup> David Reyes,<sup>2</sup> Travis Wade,<sup>3</sup> Tore Niermann,<sup>4</sup> Jonas Krehl,<sup>1</sup> Benedicte Warot-Fonrose,<sup>2</sup> Bernd Büchner,<sup>1</sup> Etienne Snoeck,<sup>2</sup> Christophe Gatel,<sup>2</sup> and Axel Lubk<sup>1</sup>

<sup>1</sup>*Institute for Solid State Research, IFW Dresden, Helmholtzstr. 20, 01069 Dresden, Germany*

<sup>2</sup>*CEMES-CNRS 29, rue Jeanne Marvig, B.P. 94347 F-31055, Toulouse Cedex, France*

<sup>3</sup>*Laboratoire des Solides Irradiés, Ecole Polytechnique, CNRS, CEA, Université Paris Saclay, F 91128 Palaiseau, France*

<sup>4</sup>*Institute for Optics and Atomic Physics, Technische Universität Berlin, Strasse des 17. Juni 135, 10623 Berlin, Germany*

Complex 3D magnetic textures in nanomagnets exhibit rich physical properties, for example in their dynamic interaction with external fields and currents, and play an increasing role for current technological challenges such as energy-efficient memory devices. To study these magnetic nanostructures including their dependency on geometry, composition and crystallinity, a 3D characterization of the magnetic field with nanometer spatial resolution is indispensable. Here we show how holographic vector field electron tomography can reconstruct all three components of magnetic induction as well as the electrostatic potential of a Co/Cu nanowire with sub 10 nm spatial resolution. We address the workflow from acquisition, via image alignment to holographic and tomographic reconstruction. Combining the obtained tomographic data with micromagnetic considerations we derive local key magnetic characteristics, such as magnetization current or exchange stiffness, and demonstrate how magnetization configurations, such as vortex states in the Co-disks, depend on small structural variations of the as-grown nanowire.

## INTRODUCTION

Novel synthesis methods and the discovery of emerging magnetic phenomena (e.g., topological non-trivial textures) at the nanoscale triggered an expansion of nanomagnetism into three dimensions (3D) focusing on unconventional magnetic configurations with unprecedented properties [1]. These nanomagnetic configurations are interesting for prospected [2] and realized applications in field sensing [3], magnetic memory, and spintronics [2, 4, 5]. Indeed, even trivial magnetic systems such as homogeneously magnetized domains adopt a 3D modulation near surfaces due to ubiquitous surface anisotropies and the role of dipolar interactions as the demagnetizing field. Surface induced modulations play a crucial role in the formation and the dynamics of different classes of domain walls in magnetic nanowires (transverse-vortex and Bloch point domain walls [5, 6]). Similarly, surfaces of chiral magnets characterized by a non-zero anti-symmetric Dzyaloshinskii-Moriya interaction (DMI) [7] exhibit 3D surface twists [8], chiral bobbles [9, 10] and other 3D textures. Conceptually similar to DMIs, handed magnetic coupling can occur in curvilinear surfaces, which can be considered as a frozen and frustrated gauge background induced by the spatially varying frame of reference. As a consequence, a family of curvature-driven effects are predicted including magnetochiral effects and topologically induced magnetization patterning, e.g., skyrmion multiplet states in bumpy films [11]. Another example pertains to magnetically frustrated 3D configurations found in (artificial) spin ice [12], where the

magnetic dipole interaction is the driving force for highly degenerated ground states.

To gain insight into 3D magnetic textures in nanomagnets, tomographic magnetization mapping techniques with spatial resolution approaching the nanometer regime are highly desired. There are, however, a limited number of contrast mechanisms, which allow to record projections of the magnetic field suitable for a tomographic reconstruction, notably, (soft) X-ray techniques and transmission electron microscopy (TEM)-based phase reconstruction techniques. Both techniques are still in their infancy with only a few studies reported so far. Soft X-ray tomography has been employed to retrieve spin textures [13] on curved magnetic films at a spatial resolution approaching 50 nm, with challenges facing the further reduction of resolution and the limited penetration depth. This could recently be solved by employing hard X-rays to tomographically reconstruct either one magnetization component [14], or two via a dual-axis approach, enabling estimation of the third [15].

The first TEM-based proof-of-principle 3D reconstruction of one Cartesian component of the magnetic induction (flux density)  $\mathbf{B}$  by employing electron holographic tomography (EHT) dates back already 25 years [16]. However, due to instrumental and computational limitations, progress in this research field was only little until five years ago, when a quantitative reconstruction of one  $\mathbf{B}$ -component in- and outside magnetic nanoscale materials was achieved [17–19]. The spatial resolution obtained in these studies is better than ten nanometers. However, further improvements in resolution will be very challenging because of fundamental detection limits for electron holography (EH) of the magnetic signal [20, 21] and experimental challenges in electron tomography. The full reconstruction of all three Cartesian com-

\* Corresponding author (d.wolf@ifw-dresden.de)

ponents, which we here refer to as holographic vector field electron tomography (VFET), remains challenging due to the complexity of acquisition and reconstruction involved. Notwithstanding, isolated studies have been reported with large regularization and reduced spatial resolution [22] or angular sampling [23]. Another challenge is to characterize the specimen in terms of magnetization  $\mathbf{M}$  instead of the  $\mathbf{B}$ -field reconstructed by EHT. Therefore micromagnetic modelling has been included in the tomographic reconstruction to retrieve the full magnetic configuration [24, 25].

In off-axis electron holography, the phase shift  $\varphi$  in the object plane  $(x, y)$  with respect to a vacuum reference acquired by an electron wave passing through a magnetic sample along  $z$  direction is given by the Aharonov-Bohm phase shift [26]

$$\varphi(x, y) = \int_{-\infty}^{+\infty} \left( \frac{e}{\hbar v} V(x, y, z) - \frac{e}{\hbar} A_z(x, y, z) \right) dz. \quad (1)$$

Here  $v$  is the electron velocity,  $V(x, y, z)$  the 3D electrostatic potential,  $e$  the elementary charge,  $\hbar$  the reduced Planck constant, and  $A_z(x, y, z)$  the 3D component of the magnetic vector potential parallel to the electron beam direction  $z$ . Accordingly, the first term can be considered as electric phase shift  $\varphi_{\text{el}}$  and the second one as magnetic phase shift  $\varphi_{\text{mag}}$ . By converting the latter to the magnetic flux enclosed between interfering paths of object and reference wave, the directional spatial derivatives of the phase are

$$\begin{aligned} \nabla_{x,y} \varphi_{\text{mag}}(x, y) &= \frac{e}{\hbar} \nabla_{x,y} \iint \mathbf{B}(\mathbf{r}) d\mathbf{S} \\ &= \frac{e}{\hbar} \int_{-\infty}^{\infty} \begin{pmatrix} B_y(\mathbf{r}) \\ -B_x(\mathbf{r}) \end{pmatrix} dz, \end{aligned} \quad (2)$$

proportional to the projected in-plane  $\mathbf{B}$ -components. The last line of the above relation also holds for inline holographic techniques, such as transport of intensity holography [22, 27, 28]. Inline techniques, however, act spatially like high-pass filters [28], i.e., are ill-conditioned for reconstructing low spatial frequencies. To separate electric and magnetic contributions in the total phase shift ( $\varphi = \varphi_{\text{mag}} + \varphi_{\text{el}}$ ), two phase images with reversed magnetic induction are required [29]. Subtracting both allows to remove the electric phase shift, which does not change sign under time-reversal as opposed to the magnetic one. To reconstruct the 3D distribution of  $\mathbf{B}$  from their projections, we collect a series of projections at different angles (tilt series) and employ tomographic reconstruction algorithms to this tilt series. By tilting about a particular axis, say  $x$ , we obtain a complete set of projections of the component  $B_x$ , whereas the remaining two components mix in their contribution to the magnetic flux as a function of tilt angle. Consequently, three tilt series around perpendicular axes are required to reconstruct the vector field  $\mathbf{B}$ . Commercially available TEM

specimen holder allow tilting only about two independent axes. Therefore, we have to exploit the solenoidal character of the  $\mathbf{B}$ -field (Gauss's law for magnetism), i.e.

$$\nabla \cdot \mathbf{B} = \partial_x B_x + \partial_y B_y + \partial_z B_z = 0, \quad (3)$$

to obtain the third component  $B_z$  (see Supplementary Note 1).

In the following, we combine all these strands, facilitating the 3D reconstruction of the magnetic induction as well as the 3D magnetization and related magnetic properties. More specifically, we demonstrate the 3D reconstruction of all three  $\mathbf{B}$ -field components with sub 10 nm resolution and derive magnetization currents and exchange energy contributions. We correlate the magnetic configuration to the chemical composition from the mean inner potential (MIP) 3D distribution reconstructed in parallel by holographic VFET. Additionally, we show how to derive  $\mathbf{M}$  from  $\mathbf{B}$  by involving micromagnetic considerations. Within the case study of a multilayered nanowire (NW) composed of alternating magnetic Co and non-magnetic Cu disks, we observe a range of different magnetic configurations including vortex states. Such structures are model systems of spintronics devices such as spin valves or spin-torque-based microwave devices, for which the knowledge and control of the initial magnetic state is crucial for applications.

## RESULTS

### Workflow of holographic vector field electron tomography

Holographic VFET, illustrated in Fig. 1, starts with the electron hologram acquisition (1, 2) and ensuing phase image reconstruction out of it (3). Then, these three steps are repeated at each tilt direction for the collection of two orthogonal tilt series of phase images (4). The latter two are separated in their electric (5) and magnetic (6) parts, and reconstructed by tomographic techniques yielding the 3D distributions of electric potential (7) as well as the two magnetic  $\mathbf{B}$ -field components  $B_x$  and  $B_y$  (8). Finally, the third magnetic  $\mathbf{B}$ -field component  $B_z$  is computed from  $\nabla \cdot \mathbf{B} = 0$  (9). In order to perform the crucial separation of electric and magnetic phase shifts (5,6), each tilt series (ideally  $360^\circ$  is split into two sub tilt series (ideally  $180^\circ$ ). However, even by using dedicated tomography TEM sample holders, in many cases the specimen and holder geometry may de facto limit the tilt range to usually  $140^\circ$ . Thus, the second sub tilt series with the corresponding opposite projections has to be recorded after the sample was turned upside-down outside the electron microscope. Consequently, tomograms reconstructed from those tilt series with incomplete tilt range suffer from a direction-dependent reduction of resolution leading to so-called missing wedge artifacts [30]. The details about acquisition, holographic

reconstruction, the elaborate post processing of projection data, tomographic reconstruction, and computation of the  $B_z$ -component are given in the Methods section at the end.

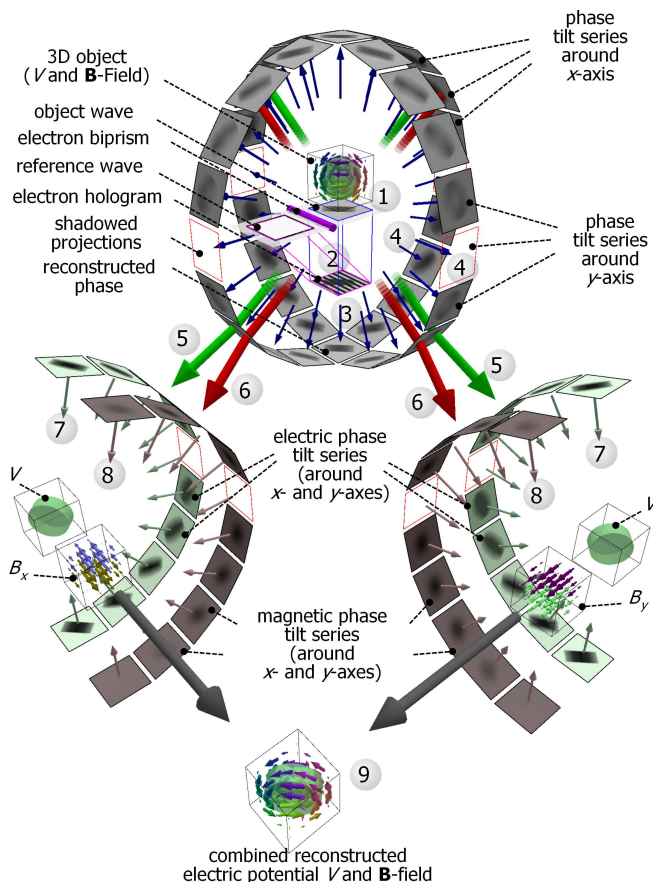


Figure 1. Principle of holographic vector field electron tomography. 1) Electron waves pass through the magnetic sample represented by both electrostatic potential  $V$  and magnetic  $\mathbf{B}$ -field. 2) Underneath the sample, an electrostatic biprism brings the modulated part (object wave) of the electron waves to interference with an unmodulated part (reference wave) resulting in an electron hologram at the detector plane. 3) The hologram is reconstructed numerically yielding the amplitude and phase shift of the object wave. 4) Rotating and recording the object around two tilt axes,  $x$  and  $y$ , provides for each tilt axis a  $360^\circ$  phase tilt series. A few projections might be missing due to technical and space limitations of the experiment. 5/6) Half the sum/difference of opposite projections (green/red arrow) results in the electric/magnetic part of the phase shift, thus two  $180^\circ$  tilt series for the tilt axes  $x$  and  $y$ . 7) The electric potential is reconstructed in 3D from the electric phase tilt series around  $x$ - or  $y$ -axis, or both results are averaged. 8) The two magnetic  $\mathbf{B}$ -field components  $B_x$  and  $B_y$  are reconstructed in 3D from the magnetic phase tilt series around  $x$ - and  $y$ -axis, respectively. 9) Finally, the 3D  $B_z$ -component is obtained by solving  $\nabla \cdot \mathbf{B} = 0$ .

### 3D magnetic induction mapping of a layered Cu/Co nanowire

Fig. 2 depicts the 3D reconstruction of a multilayered Co/Cu NW using holographic VFET. The bright-field TEM image shown in Fig. 2a reveals the nanocrystalline structure of the NW, but does not visualize the alternating Co and Cu segments as intended by template-based electrodeposition growth (Fig. 2b). Fig. 2c shows the 3D  $\mathbf{B}$ -field reconstructed from the magnetic phase shift in combination with the MIP obtained from the electric phase shift distribution reflecting the composition of the nanowire. The positions of the stacked Co and Cu disks (visible due to the difference in the MIP between Co and Cu) are also confirmed by energy-filtered TEM (EFTEM) on exactly the same NW (see Supplementary Note 2). Previous quantitative EFTEM investigations on similar NWs have also demonstrated the presence of 15% of Cu in the Co disks resulting from the electrodeposition [31]. We obtained MIP values for the Co (incl. 15% Cu) and Cu disks of  $V_0^{\text{Co}} = (21 \pm 1) \text{ V}$  and  $V_0^{\text{Cu}} = (17.5 \pm 1) \text{ V}$ , respectively by determining the peak maximum and width in the histograms evaluated at the corresponding tomogram regions. The MIP tomogram (Fig. 2c and Supplementary Movie 1) already provides an important contribution for a better analysis of magnetic properties, because it reveals that the Co disks not only deviate slightly from their nominal thickness of 25 nm and their cylindrical shape intended by electrodeposition synthesis (see Methods section for the details), but also vary to some degree in the inclination angle along the growth direction. Therefore, to illustrate the 3D distribution of the  $\mathbf{B}$ -field within the individual Co disks, we selected cross-sections oriented parallel to their inclined base surface (Figs. 2c,d and Supplementary Movie 2). Accordingly, two different magnetic configurations were observed: A homogeneously in-plane magnetized state and a vortex state. The latter shows both clock-wise and counter-clock-wise rotation without noticeable correlation of the rotation between the Co-disks (i.e., coupling between different rotational directions). At the center of the vortex, the magnetization (and hence the  $\mathbf{B}$ -field) is expected to rotate out-of-plane within a core radius smaller than 10 nm (see further below for details), which is, however, difficult to resolve unambiguously in the vector tomogram at the present spatial and signal resolution. These out-of-plane magnetized vortex cores together with other out-of-plane components, such as Co bridges in the Cu (e.g., between disks 1 and 2, 7 and 8 in Fig. 2e) and asymmetries of the vortices with respect to the NW axis, may, however, contribute to an Aharonov-Bohm phase shift in the vacuum region around the NW. This is demonstrated in Supplementary Note 3, where the reconstructed 3D magnetic structure is correlated with a corresponding phase image: An inspection of the vacuum region in the phase image reveals that the core polarities are mutually aligned by their long-range dipole interaction (producing a net flux density along the

NW), while the in-plane states (disks 2 and 7) emanate particularly strong stray fields. We finally observe some out-of-plane modulations outside of the core region as indicated by yellow and black color in (Fig. 2d), which will be discussed in detail further below. Turning to the longitudinal cross section (Fig. 2e) we notice the strong reduction of the magnetic induction between the vortex state discs (producing small stray fields only). Correspondingly, significant  $\mathbf{B}$ -fields are visible in the vicinity of the in-plane magnetized discs producing large stray fields. The longitudinal section also exhibits the out-of-plane modulations of the vortex states and indicates a complicated configuration in the NW tip, which will not be discussed further in detail. In order to examine the reliability and fidelity of these delicate findings, we measured the spatial resolution of the tomograms by Fourier shell correlation (FSC) [32]. As described in Supplementary Note 4, we determined with FSC a spatial resolution of about 7 nm for the 3D reconstructions of both  $B_x$  and  $B_y$ , and of about 5 nm in case of the 3D electrostatic potential. In addition, we verified the fidelity of the reconstructed  $\mathbf{B}$ -field by applying our holographic VFET reconstruction on a simulated magnetic Co disk with similar magnetization, dimension, orientation, configuration (vortex and in-plane magnetized) and sampling as in the experiment (Supplementary Note 5). The resulting  $\mathbf{B}$ -field tomograms agree very well with their simulated input data, even though a limited tilt range is used ( $\pm 70^\circ$ ). Our VFET analysis can thus unambiguously reveal the 3D magnetic structure of a complex system, highlights the various magnetic configurations and determine magnetic characteristics such as the vorticity and out-of-plane modulations of a vortex.

### Magnetization current exchange density

In the following we elaborate on the relation of other important magnetic quantities to the  $\mathbf{B}$ -field, in order to comprehensively characterize the nanomagnetic properties of the NW. We first note that the conservative (longitudinal) and solenoidal (transverse) part of the Helmholtz decomposition of the magnetization (with scalar magnetic potential  $\Phi$  and vector potential  $\mathbf{A}$ )

$$\mathbf{M} = \underbrace{\nabla \Phi}_{-\mathbf{H}} + \underbrace{\mu_0^{-1} \nabla \times \mathbf{A}}_{\mu_0^{-1} \mathbf{B}} \quad (4)$$

directly correspond to the magnetic field and magnetic induction. As holographic VFET reconstructions cannot reconstruct the conservative part (i.e.,  $\mathbf{H}$ , which is typically large at boundaries, interfaces but also in Néel textures), the magnetization  $\mathbf{M}$  cannot be unambiguously retrieved from VFET without additional knowledge about the magnetism of the sample. In order to elaborate on this crucial point, we first compute the total current density  $\mathbf{j} = \mu_0^{-1} \nabla \times \mathbf{B}$ , i.e., the vorticity of the magnetic induction. If we decompose  $\mathbf{j}$  into free and magnetization

(or bound) currents ( $\mathbf{j} = \mathbf{j}_f + \mathbf{j}_b$ ) and take into account that the former can be neglected in the magnetostatic limit, we obtain the magnetization current from

$$\mathbf{j}_b = \nabla \times \mathbf{M} = \mu_0^{-1} \nabla \times \mathbf{B}, \quad (5)$$

which appears in various energy terms of the micromagnetic free energy. In our case, the three most important micromagnetic energy contributions determining the remanent state in the stacked NW are the exchange, demagnetizing field, and crystallographic anisotropy energy

$$E_{\text{tot}}[\mathbf{M}] = E_{\text{ex}}[\mathbf{M}] + E_{\text{d}}[\mathbf{M}] + E_{\text{a}}[\mathbf{M}]. \quad (6)$$

The magnetization current contributes among others to the exchange energy (see Supplementary Note 6 for detailed expressions of  $E_{\text{d}}$  and  $E_{\text{a}}$ )

$$\begin{aligned} E_{\text{ex}}[\mathbf{M}] &= \frac{A}{M_s^2} \int \left( (\nabla \cdot \mathbf{M})^2 + |\nabla \times \mathbf{M}|^2 \right) dV \quad (7) \\ &= \frac{A}{M_s^2} \int \left( (\rho_m)^2 + |\mathbf{j}_b|^2 \right) dV \end{aligned}$$

with exchange stiffness  $A$ , and saturation magnetization  $M_s$ . Therein, the first term denotes the magnetic charge contribution ( $\rho_m = -\nabla \cdot \mathbf{M} = \Delta \Phi$ ), and additional terms describing surface contributions not written out here (see Methods section and Supplementary Note 6 for further details). Consequently, exchange energy minimization favours suppression of both magnetic charge and magnetization current in the volume. The 3D distribution of the magnetization current exchange density  $|\mathbf{j}_b|^2$  in the Co/Cu NW is computed from the reconstructed  $\mathbf{B}$ -field using Eq. 5, and correlated with the MIP tomogram (Fig. 3a). As a result, the current exchange density is effectively minimized in the homogeneously magnetized parts (slices 2,7 in Figs. 3b,c). In contrast, it is significantly larger in the vortex regions (slices 1,3-6,8 in Figs. 3b,c), which is, of course, compensated by the decrease in demagnetizing field and energy in the total energy functional.

### Comparison with micromagnetic simulations

The above considerations now open a way to derive  $\mathbf{M}$  from  $\mathbf{B}$  by incorporating micromagnetic modelling. At the example of the symmetric magnetic exchange energy (Eq. (7), see Supplementary Note 6 for the other energy contributions), we see that the micromagnetic energy functional can be reduced to a functional of a scalar field (i.e., the magnetostatic potential  $\Phi$ ),  $E_{\text{tot}}[\mathbf{M}] \rightarrow E_{\text{tot}}[\Phi]$ , if  $\mathbf{B}$  (and hence  $\mathbf{j}_b$ ) is known (from the experiment). This significantly reduces the degrees of freedom and hence the complexity of the micromagnetic minimization problem of  $E_{\text{tot}}$ , which can be exploited in various ways for retrieving  $\mathbf{M}$ . First, micromagnetic simulations can be used to compute  $\mathbf{B}$  from a given  $\mathbf{M}$  and iterate over different magnetization configurations until

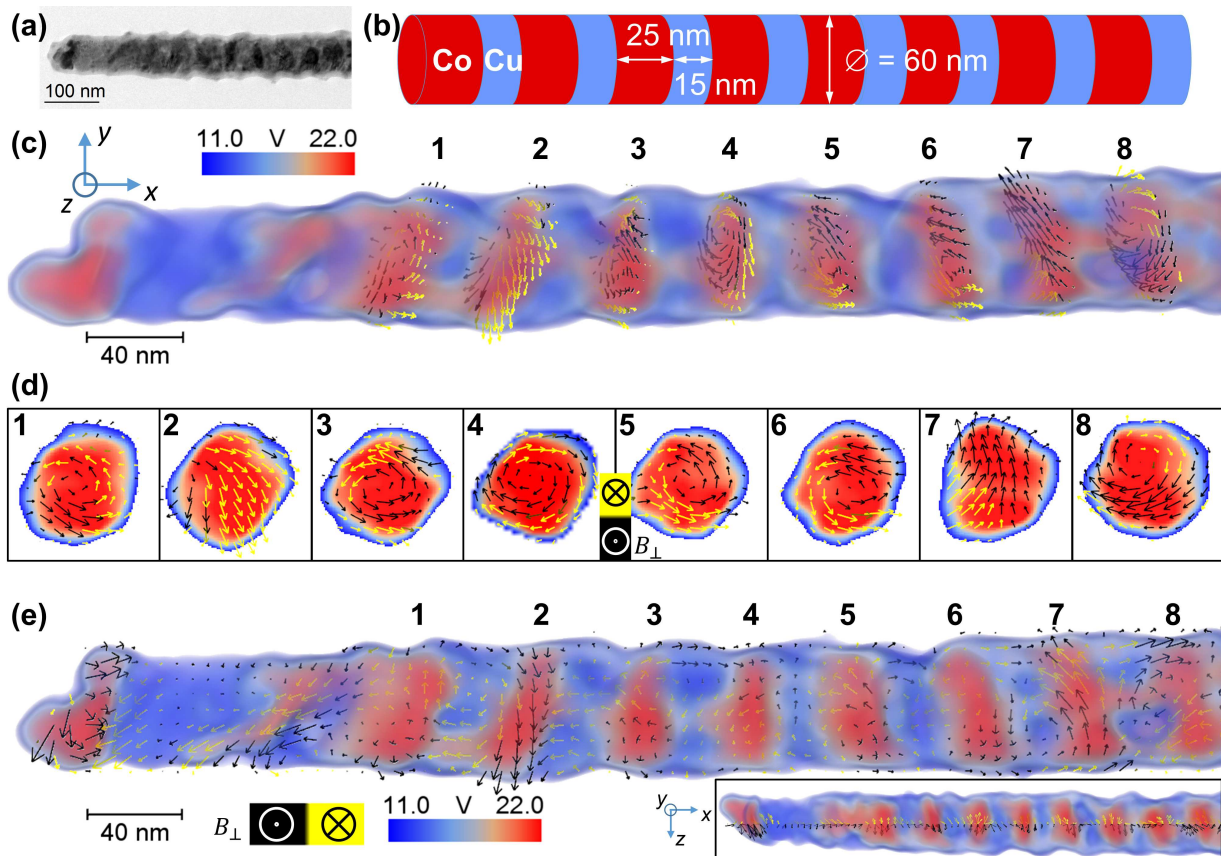


Figure 2. 3D reconstruction of multilayered Co/Cu nanowire (NW). (a) Bright-field transmission electron micrograph of the NW. (b) Idealized model of the NW as intended by template-based electrodeposition growth. (c) The volume rendering of the NW's mean inner potential (MIP) displays Co in red and Cu in bluish-white (as illustrated in (b)). The arrow plots represent the field lines of magnetic induction ( $\mathbf{B}$ -field) sliced through eight Co disks, where the direction of the normal  $\mathbf{B}$ -field component is color-coded in black and yellow. Please note that the coordinate system is rotated with respect to the experimental setup: The  $B_x$  component is now parallel to the NW axis (=out-of-plane component of disks). (d) Slices through the Co disks as indicated in (c): Co disks 2,7 show in-plane magnetization, 1,3,5,6 counter-clock-wise, and 4,8 clock-wise vortex magnetization. (e) Same viewing direction as (c), but arrow plot taken in axial NW-direction. The inset illustrates where the arrow plot intersects the NW.

agreement with the reconstructed data is reached. We use this approach below to obtain information about the exchange stiffness and magnetocrystalline anisotropy in the stacked NW. Second, micromagnetic simulation can be adapted such to directly minimize the energy as a function of the scalar field  $\Phi$ . Such adapted micromagnetic schemes, which even allow to analytically derive the total magnetization  $\mathbf{M}$  for highly symmetric magnetic configurations, are further discussed in Supplementary Note 6.

In the light of the above discussion, we now employ micromagnetic simulations to gain more insight into the complex magnetic structure of the Co/Cu NW (see Methods section and Supplementary Note 7 for details). In order to foresee which kind of magnetic remanent states could be obtained in such layers, we first simulated the remanent state phase diagram of a single Co disk as a function of thickness and diameter (Fig. 4a). To mimic the experimental conditions, remanent states were cal-

culated after saturation with 1 T close to the wire axis. Simulations were performed with the magnetic parameters of Ref. [31] and a tilt angle of the layers of about  $10^\circ$  with respect to the wire axis. Depending on the ratio of thickness and diameter, the remanent states of a single layer can be out-of-plane, in-plane or vortices with the core either being out-of-plane or tilted with respect to the normal of the layers. The Co disks of the investigated NW are at the boundary of the in-plane and vortex configurations, which agrees well with the coexistence of both configurations in the experiment. Additional contributions such as dipolar coupling between the discs, multiple grains including magnetocrystalline and surface anisotropies, coupling to defects, irregular disc shapes and chemical gradients further influence the magnetic state of a real Co disc. In particular the contribution of the crystallographic anisotropy is very complex in the Co (alloyed with 15% Cu) disks including randomly oriented nanoscaled grains of predominant fcc

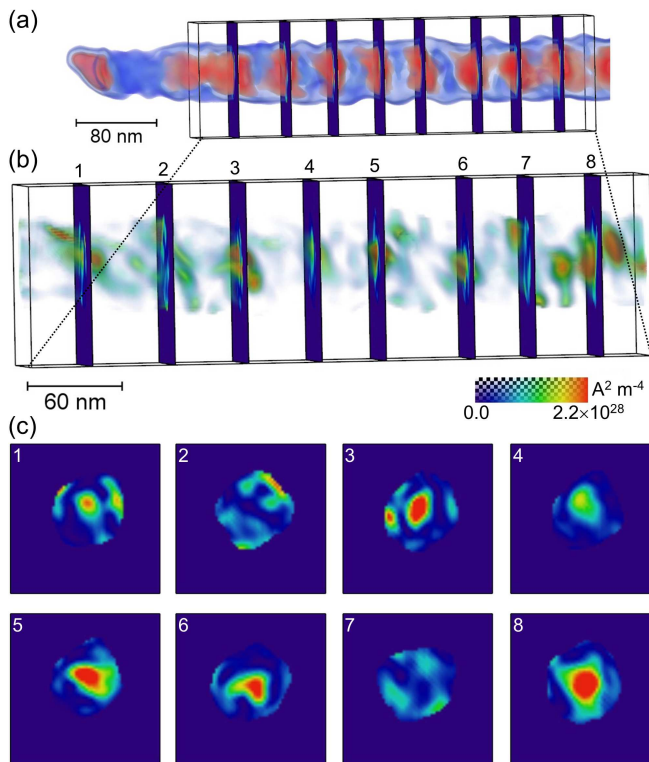


Figure 3. Magnetization current exchange density. (a) 3D mean inner potential tomogram of the Co/Cu nanowire with bounding box indicating the region where the current exchange density is computed. (b) Volume rendering of the current exchange density. (c) Slices through Co disks 1-8, in which the Co disks with a vortex state (1, 3-6, and 8) exhibit a localized maximum in the current exchange density.

symmetry (i.e., cubic anisotropy). Using TEM, the nanocrystallinity can be observed by local diffraction contrast of the nanometer-sized grains when they are oriented in low-index zone axis with respect to the electron beam direction. This is visible in the bright-field TEM image (Fig. 2a) and also in the original electron holograms, from which the tomograms are reconstructed (Supplementary Note 8). Therefore, to go deeper in the analysis of the magnetic properties of the layers, we performed simulations of the eight Co layers shown in Figs. 4b,c. Within the simulations the magnetization amplitude  $M_s$ , exchange constant  $A$  and crystalline anisotropy  $H_K$  of each Co layer were changed until the best fit to the experiment was achieved. A crucial step is to implement the 3D morphology of the layers extracted from the MIP tomogram into the micromagnetic simulations (see Methods section and Supplementary Note 7) in order to take into account the geometrical symmetry breaking and inhomogeneity of the Co layers in the calculations. This valuable input significantly reduces the numbers of unknown parameters to reproduce the magnetic configurations in the simulations, and allowed to extract magnetic parameters for all individual layers within a range for  $M_s$  (1000 – 1200)  $\text{Am}^{-1}$ ,  $A$  (12 – 20)  $10^{-12} \text{ Jm}^{-1}$ , and  $H_K$

(50 – 130)  $10^3 \text{ Jm}^{-3}$  (see Supplementary Table 2 for values of each layer). The variation of these intrinsic parameters from one layer to the other reflects the large impact of the individual disc shapes in the formation of the magnetic configurations. Note, however, the magnetization is found to be between 20 and 30% overestimated in our simulations (Fig. 4c), which indicates that the magnetization amplitude and most probably the exchange constant for each layer can be decreased even further. Such low values of magnetic constants due to the Cu impurities in the Co layers were also observed in a recent work [33] on electrodeposited Co/Cu multilayers grown in a single bath, especially when decreasing the thickness of the layer.

## DISCUSSION

We have demonstrated the successful 3D reconstruction of both the magnetic induction vector field and 3D chemical composition of a complex real nanomaterial with sub-10 nm spatial resolution using holographic VFET. Crucial steps are the semi-automated holographic acquisition of dual-axis tilt series within a tilt range of  $280^\circ$ , holographic phase reconstruction, precise image alignment, separation of electric and magnetic phase shift, the tomographic reconstruction of all three  $\mathbf{B}$ -field components exploiting the constraint  $\nabla \cdot \mathbf{B} = 0$ . Moreover, we elaborated on the extraction of magnetic properties such as the solenoidal magnetic exchange energy from the tomographic data. The results obtained from a multilayered Co/Cu NW paint a complex picture of the 3D magnetization behaviour, for example, the coexistence of vortex and in-plane magnetized states. This allows to set up a micromagnetic model including the exact geometry of the Co nanodisks that matches the experimental  $\mathbf{B}$ -field tomogram, from which magnetic parameters of individual layers can be derived. Indeed, micromagnetic simulations of nano-objects are generally performed considering “ideal” systems, which can lead to false predictions of the magnetic states. Avoiding problems of geometrical uncertainties as well as providing additional data in terms of 3D  $\mathbf{B}$ -field distribution for optimizing micromagnetic simulation is therefore a great advance for a precise analysis of the magnetic properties of nano-objects. We anticipate further improvements by including additional tilt series (e.g., utilizing improved 3-tilt axis tomography holders), increased signal-to-noise ratio (SNR) at long exposure times using automated feedback of the microscope [34], improved vector field reconstruction schemes and adapted micromagnetic modeling of the magnetostatic potential, explicitly exploiting the a priori knowledge of the  $\mathbf{B}$ -field. The technique holds large potential for revealing complex 3D nanomagnetization patterns, e.g., in chiral magnets, nanomagnets (e.g, NWs) and frustrated magnets, currently not possible with other methods at the required spatial resolution.

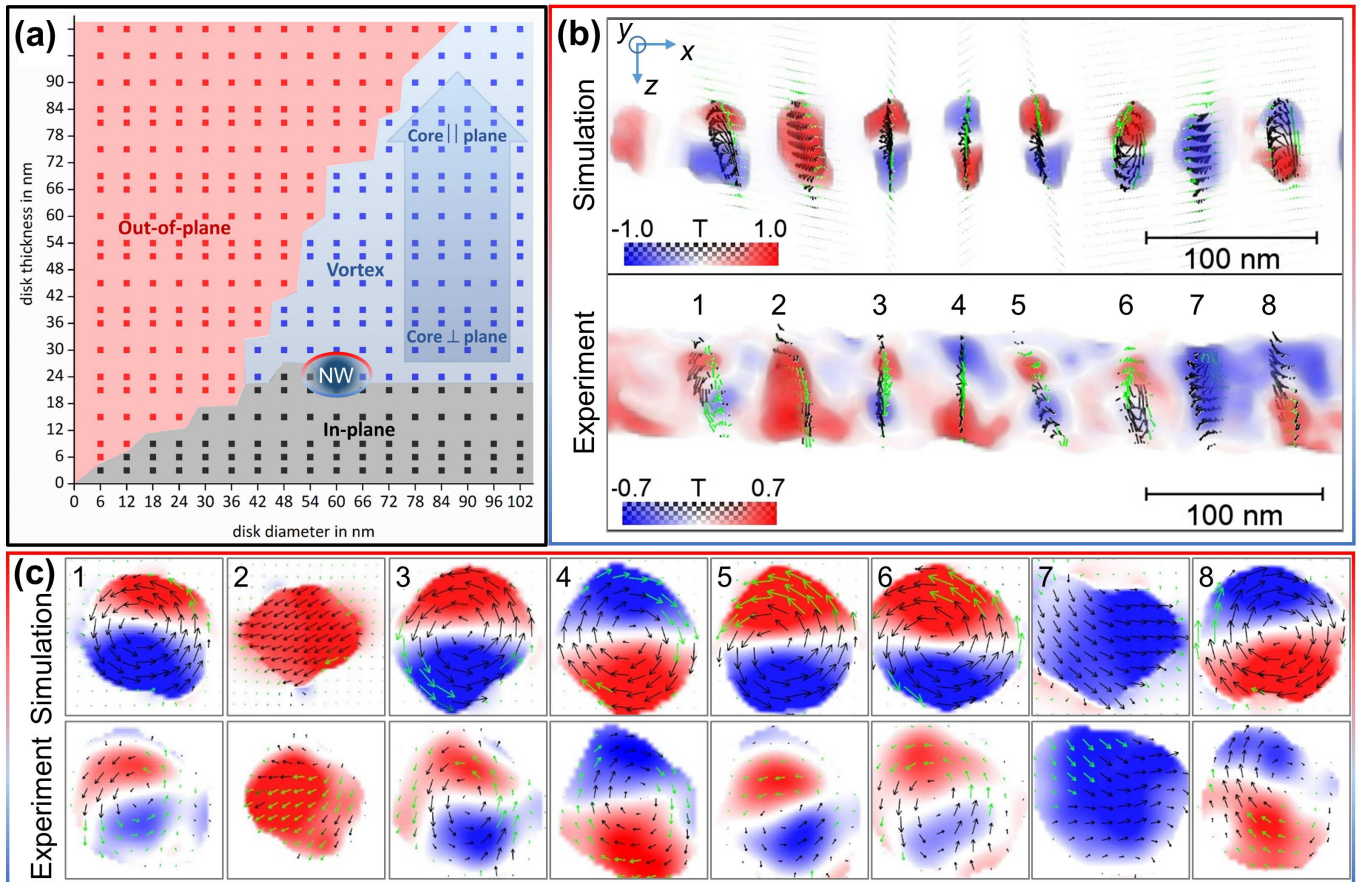


Figure 4. Micromagnetic simulations. (a) Simulated magnetic phase diagram of regular Co disks/cylinders obtained by variation of diameter and thickness. Each point (square) corresponds to the resulting magnetic state obtained from one micromagnetic simulation. The region of the investigated nanowire (NW) is highlighted around 60nm diameter and 25 nm thickness. (b) Comparison of the  $B_y$  component between the simulated and experimental Co/Cu NW. In the simulation, the irregular morphology of the Co disks obtained from the mean inner potential tomogram was taking into account. Note the different blue-red color-coding range between simulation and experiment according to the color bars. (c) Slices through the Co disks 1-8 as indicated in (b) superimposed by an arrow plot indicating the magnetic state. The opposite out-of-plane directions are distinguished by black and green as also shown in the arrowplots in (b).

## METHODS

### Nanowire Synthesis

NWs are grown via template-based electrodeposition technique. The thereby used template was a commercial polycarbonat membrane (Maine Manufacturing, LLC). NWs with diameter ranging from 55 to 90 nm are obtained by electrodeposition in pulse mode from a single bath containing both Co and Cu ions. The deposition potentials for Co and Cu are  $-1$  V and  $-0.3$  V, respectively. Lower deposition potential of the Co leads to about 15% of Cu impurities inside the Co layers [31]. The duration of the deposition potential pulses was adjusted to 1 s for Co and 10 s for Cu, to achieve nominal layer thicknesses of 25 nm Co and 15 nm Cu. In order to be transferred onto a holey carbon grid for TEM experiments, the membrane surrounding the wires was removed by immersion

of the sample in dichloromethane. All details about the growth and cleaning processes are given in Ref. [31] and references therein. Prior to the tomography experiments, the NWs were saturated in a 1T magnetic field oriented roughly at  $10^\circ$  from the wire axis direction.

### Acquisition of holographic tilt series

The holographic tilt series was recorded at the FEI Titan 80-300 Holography Special Berlin TEM instrument, in image-corrected Lorentz-Mode (conventional objective lens turned off) operated at 300 kV. We employed the two electron biprism setup [35] that was adjusted by an upper biprism voltage of 35 V, a lower biprism voltage of 100 V, and an intermediate X-lens (extra lens between the two biprisms) excitation of  $-0.36$ . For acquisition of electron holgrams, a 2k by 2k slow scan CCD camera (Gatan Ultrascan 1000 P) was used. The high tilt an-

gles, and the manual in-plane rotation of the sample in between the two tilt series (one to reconstruct  $B_x$  and one to reconstruct  $B_y$ ), were achieved by means of a dual-axis tomography holder (Model 2040 of E. A. Fischone Instruments, Inc.). The acquisition process was performed semi-automatically with an in-house developed software package for an efficient collection of holographic tilt series consisting of object and object-free empty hologram [36]. The latter is required for correction purposes as explained below. For the first tilt series, the specimen was rotated in-plane, such that an angle between NW axis and tilt axis of  $+44.5^\circ$  was obtained. For the second tilt series, the specimen was rotated further in-plane by  $91^\circ$  (ideal is  $90^\circ$ ) resulting in an angle between NW axis and tilt axis of  $-46.5^\circ$ . After turning the sample upside down ex-situ, two more holographic tilt series were recorded that represent the flipped version of the first two tilt series. The tilt range of each tilt series was from  $-69^\circ$  to  $+66^\circ$  in  $3^\circ$  steps. The electron holograms had an average contrast of 14% in vacuum, a fringe spacing of 3.3 nm, a field of view of  $1\ \mu\text{m}$ , and a pixel size of 0.48 nm.

### Reconstruction and processing of projection data

The elaborate image data treatment was mainly accomplished using in-house developed scripts and software plugins for Gatan Microscopy Suite (GMS). Amplitude and phase images were reconstructed by filtering out one sideband of the Fourier transform of the electron hologram, e.g., described in Ref. [37]). Likewise, amplitude and phase images were reconstructed from empty holograms for correction of imaging artifacts, such as distortions of camera and projective lenses. In detail, we used a soft numerical aperture with a full width at half maximum of  $1/9\ \text{nm}^{-1}$ , and zero-damping the signal at  $1/4.5\ \text{nm}^{-1}$ . Accordingly, the resolution (reconstructed pixel size) of the image wave after inverse Fourier transformation (FT) of the cut sideband is in the range from 4.5 nm to 9 nm depending on the SNR. After holographic reconstruction of all four tilt series, phase images were unwrapped with automatic phase unwrapping algorithms (Goldstein or Flynn) [38]. Possible artifacts after application of these algorithms at regions, where the phase signal is too noisy or undersampled, are corrected by manual treatment of using preknowledge of the phase shift (e.g. from adjacent projections) [39]. All four phase tilt series were prealigned separately by cross-correlation to correct for coarse displacements between successive projections. Furthermore, those two tilt series, where the sample was flipped before acquisition, were flipped back numerically yielding for each tilt angle a pair of phase images with equal electric but opposite magnetic phase shift. Then, each pair of phase images was aligned by applying a linear affine transformation on the “flipped” phase image, which considers displacements, rotation, and direction-dependent magnification changes [18]. After this step, the separation of electric and magnetic phase shifts was

performed for these pairs of phase images as illustrated in Fig. 1, steps (5) and (6). To finally employ the fine alignment (i.e., the accurate determination of the tilt axis and correction for subpixel displacement), we used a self-implemented center-of-mass method for correction of displacements perpendicular to the tilt axis and the common line approach [40] for the correction of displacements parallel to the tilt axis. We applied these procedures initially on the electric phase tilt series, which has a higher SNR than the magnetic one, and used the thereby determined displacements for alignment of magnetic phase tilt series. Before computation of the derivatives, the magnetic phase images were smoothed slightly by a non-linear anisotropic diffusion (NAD)[41] filter using the Avizo software package (ThermoFisher Scientific Company). Following Eq. 2, we calculated the projected  $B_x$ - and  $B_y$ - components from the derivatives of the magnetic phase images in  $y$ - and  $x$ - direction.

### Tomographic reconstruction

The tomographic reconstruction of electrostatic potential,  $B_x$ - and  $B_y$ - component from their aligned tilt series (projections) was conducted with the weighted simultaneous iterative reconstruction technique (W-SIRT) [42]. Since the W-SIRT involves a weighted (instead of a simple) back-projection for each iteration step, it converges faster than a conventional SIRT algorithm. The number of iterations was determined to five, by visually inspecting the trade-off between spatial resolution and noise. In addition, we reduced the missing wedge artifacts in the tomograms at low spatial frequencies by a finite support approach, explained in Ref. [43].

### Calculation of the third magnetic B-field component

In order to determine the third  $\mathbf{B}$ -field component  $B_z$  not directly obtainable from one of the two tilt series around  $x$  or  $y$ , two strategies may be applied. First, it is possible to solve third Maxwell’s law  $\text{div}\mathbf{B} = 0$  with appropriate boundary conditions on the surface of the reconstruction volume. Second, it is possible to compute the projected component of the  $\mathbf{B}$ -field perpendicular to the tilt axis in one tilt series (say around  $x$ ), which is a mixture of the  $y$  and  $z$  component in the non-rotated laboratory frame and substitute the  $y$  component with the reconstruction from the second tilt series around  $y$ . The second approach may be implemented in both a field- and vector potential-based reconstruction scheme (automatically implying  $\text{div}\mathbf{B} = 0$ ) [44]. Indeed, the two strategies to determine  $B_z$  are identical as demonstrated in the Supplementary Note 1.

The most straight-forward way to calculate  $B_z$  from Eq. 3 is by integration along the  $z$ -coordinate, that is,

$$B_z(x, y, z) = - \int_{-\infty}^z (\partial_x B_x(x, y, z') + \partial_y B_y(x, y, z')) dz'. \quad (8)$$

However, to reduce accumulation of errors while integrating along  $z$ , we employed periodic boundary conditions for solving this differential equation, which reads in Fourier space

$$B_z(x, y, z) = \mathcal{F}^{-1} \left\{ -\frac{k_x}{k_z} \mathcal{F} \{B_x\} - \frac{k_y}{k_z} \mathcal{F} \{B_y\} \right\}. \quad (9)$$

Here  $\mathcal{F} \{ \}$  and  $\mathcal{F}^{-1} \{ \}$  denote the forward and inverse 3D FT, and  $k_x, k_y, k_z$  the reciprocal coordinates in 3D Fourier space. The zero frequency component (integration constant) was fixed by setting the average of  $B_z$  to zero on the boundary of the reconstruction volume.

### Micromagnetics

Micromagnetic simulations of the remanent magnetic states were performed with Object Oriented Micromagnetic Framework (OOMMF) software package [45] solving the non-linear minimization problem (non-linear constraint  $|\mathbf{M}| = M_s$ ) of the energy functional (Eq. 6) containing the exchange, demagnetizing field and crystalline anisotropy energy as the main contributions in our case.

The details of the single disc simulations are given in the Supplementary Note 7. The 3D morphology of the Co/Cu layers is revealed from MIP tomogram by assigning each voxel to a different material region. The NW's 3D shape is segmented by a MIP threshold of 11.0 V to distinguish between NW and vacuum, whereas a MIP threshold of 18.5 V was employed to distinguish between Co ( $> 18.5$  V) and Cu ( $\leq 18.5$  V). Then, the 3D data array is interpolated to a grid with voxels of  $2 \times 2 \times 2 \text{ nm}^3$  (grid dimension:  $960 \times 160 \times 200 \text{ nm}^3$ ). Each Co layer is attributed to an individual set of magnetic parameters such as magnetization  $M_s$ , exchange constant  $A$  and uniaxial crystal anisotropy  $H_K$  (see Supplementary Table 2). Here, the assumption of uniaxial anisotropy relies on the polycrystalline nature of the layers, which may be approximated by an average anisotropy in a first order approximation. The magnetic induction  $\mathbf{B}$  in each layer is obtained summing the calculated magnetization components and the demagnetization field  $\mathbf{H}$ .

### DATA AVAILABILITY

The data that support the findings of this study are available from the corresponding author upon reasonable request.

### REFERENCES

- 
- [1] Fernandez-Pacheco, A., Streubel, R., Fruchart, O., Hertel, R., Fischer, P., and Cowburn, R. P. *Nat Commun* **8**, 15756 (2017).
- [2] Parkin, S. S., Hayashi, M., and Thomas, L. *Science* **320**, 190–194 (2008).
- [3] Karnaushenko, D., Karnaushenko, D. D., Makarov, D., Baunack, S., Schäfer, R., and Schmidt, O. G. *Advanced Materials* **27**, 6582–6589 (2015).
- [4] Hoffmann, A. and Bader, S. D. *Physical Review Applied* **4**, 047001 (2015).
- [5] Fruchart, O., Wartelle, A., Trapp, B., Stano, M., Thirion, C., Bochmann, S., Bachmann, J., Foerster, M., Aballe, L., Mentès, O., Locatelli, A., Sala, A., Cagnon, L., and Toussaint, J.-C. *arXiv:1806.10918 [cond-mat]* (2018).
- [6] Biziere, N., Gatel, C., Lassalle-Balier, R., Clochard, M. C., Wegrowe, J. E., and Snoeck, E. *Nano Lett* **13**, 2053–2057 (2013).
- [7] Bogdanov, A. N. and Yablonskii, D. A. *Zh. Eksp. Teor. Fiz.* **95**, 178–182 (1989).
- [8] Rybakov, F. N., Borisov, A. B., and Bogdanov, A. N. *Physical Review B - Condensed Matter and Materials Physics* **87**, 094424 (2013).
- [9] Rybakov, F. N., Borisov, A. B., Blügel, S., and Kiselev, N. S. *New Journal of Physics* **18**, 045002 (2016).
- [10] Zheng, F., Rybakov, F. N., Borisov, A. B., Song, D., Wang, S., Li, Z.-A., Du, H., Kiselev, N. S., Caron, J., Kovacs, A., Tian, M., Zhang, Y., Blügel, S., and Dunin-Borkowski, R. E. *Nature Nanotechnology* **13**, 451–455 (2018).
- [11] Kravchuk, V. P., Sheka, D. D., Kákay, A., Volkov, O. M., Röfller, U. K., van den Brink, J., Makarov, D., and Gaididei, Y. *Phys. Rev. Lett.* **120**, 067201 (2018).
- [12] Nisoli, C., Moessner, R., and Schiffer, P. *Rev. Mod. Phys.* **85**, 1473–1490 (2013).
- [13] Streubel, R., Kronast, F., Fischer, P., Parkinson, D., Schmidt, O. G., and Makarov, D. *Nature Communications* **6**, 7612 (2015).
- [14] Suzuki, M., Kim, K.-J., Kim, S., Yoshikawa, H., Tono, T., Yamada, K. T., Taniguchi, T., Mizuno, H., Oda, K., Ishibashi, M., Hirata, Y., Li, T., Tsukamoto, A., Chiba, D., and Ono, T. *Applied Physics Express* **11**, 036601 (2018).
- [15] Donnelly, C., Gliga, S., Scagnoli, V., Holler, M., Raabe, J., Heyderman, L. J., and Manuel Guizar-Sicairos. *New Journal of Physics* **20**, 083009 (2018).
- [16] Lai, G., Hirayama, T., Fukuhara, A., Ishizuka, K., Tanji, T., and Tonomura, A. *Journal of Applied Physics* **75**, 4593–4598 (1994).
- [17] Lubk, A., Wolf, D., Simon, P., Wang, C., Sturm, S., and Felser, C. *Applied Physics Letters* **105**, 173110 (2014).
- [18] Wolf, D., Rodriguez, L. A., Beche, A., Javon, E., Serrano, L., Magen, C., Gatel, C., Lubk, A., Lichte, H., Bals,

- S., Van Tendeloo, G., Fernandez-Pacheco, A., De Teresa, J. M., and Snoeck, E. *Chem Mater* **27**, 6771–6778 (2015).
- [19] Simon, P., Wolf, D., Wang, C., Levin, A. A., Lubk, A., Sturm, S., Lichte, H., Fecher, G. H., and Felser, C. *Nano Lett* **16**, 114–120 (2016).
- [20] Lichte, H. *Ultramicroscopy* **108**, 256–262 (2008).
- [21] Röder, F., Lubk, A., Wolf, D., and Niermann, T. *Ultramicroscopy* **144**, 32–42 (2014).
- [22] Phatak, C., Petford-Long, A. K., and De Graef, M. *Phys. Rev. Lett.* **104**, 253901 (2010).
- [23] Tanigaki, T., Takahashi, Y., Shimakura, T., Akashi, T., Tsuneta, R., Sugawara, A., and Shindo, D. *Nano Letters* **15**, 1309–1314 (2015).
- [24] Caron, J. *Model-based reconstruction of magnetisation distributions in nanostructures from electron optical phase images*, volume 177 of *Key Technologies*. Forschungszentrum Jülich GmbH Zentralbibliothek, Verlag Jülich, (2018).
- [25] Mohan, K. A., Kc, P., Phatak, C., De Graef, M., and Bouman, C. A. *IEEE Transactions on Computational Imaging* **4**, 432–446 (2018).
- [26] Aharonov, Y. and Bohm, D. *Physical Review* **115**, 485–491 (1959).
- [27] Teague, M. *Journal of the Optical Society of America* **73**, 1434–1441 (1983).
- [28] Lubk, A. In *Advances in Imaging and Electron Physics*, volume 206. (2018).
- [29] Kasama, T., Dunin-Borkowski, R., and Beleggia, M. *Electron Holography of Magnetic Materials*. InTech (2011).
- [30] Midgley, P. A. and Weyland, M. *Ultramicroscopy* **96**, 413–431 (2003).
- [31] Reyes, D., Biziere, N., Warot-Fonrose, B., Wade, T., and Gatel, C. *Nano Lett* **16**, 1230–1236 (2016).
- [32] van Heel, M. and Schatz, M. *J Struct Biol* **151**, 250–262 (2005).
- [33] Ogrodnik, P., Vetro, F. A., Frankowski, M., Checinski, J., Stobiecki, T., Barnas, J., and Ansermet, J.-P. *Journal of Physics D: Applied Physics* **52**, 065002 (2019).
- [34] Gatel, C., Dupuy, J., Houdellier, F., and Hytch, M. J. *Applied Physics Letters* **113**, 133102 (2018).
- [35] Harada, K., Tonomura, A., Togawa, Y., Akashi, T., and Matsuda, T. *Applied Physics Letters* **84**, 3229–3231 (2004).
- [36] Wolf, D., Lubk, A., Lichte, H., and Friedrich, H. *Ultramicroscopy* **110**, 390–399 (2010).
- [37] Lehmann, M. and Lichte, H. *Microsc Microanal* **8**, 447–466 (2002).
- [38] Ghiglia, D. C. and Pritt, M. D. *Two-dimensional phase unwrapping: Theory, algorithms and software*. Wiley & Sons, New York NY, (1998).
- [39] Lubk, A., Wolf, D., Prete, P., Lovergine, N., Niermann, T., Sturm, S., and Lichte, H. *Physical Review B* **90**, 125404 (2014).
- [40] Penczek, P. A., Zhu, J., and Frank, J. *Ultramicroscopy* **63**, 205–218 (1996).
- [41] Frangakis, A. S. and Hegerl, R. *J Struct Biol* **135**, 239–250 (2001).
- [42] Wolf, D., Lubk, A., and Lichte, H. *Ultramicroscopy* **136**, 15–25 (2014).
- [43] Wolf, D., Hubner, R., Niermann, T., Sturm, S., Prete, P., Lovergine, N., Buchner, B., and Lubk, A. *Nano Lett* **18**, 4777–4784 (2018).
- [44] Phatak, C., Beleggia, M., and De Graef, M. *Ultramicroscopy* **108**, 503–513 (2008).
- [45] Donahue, M. J.; Porter, D. G. *OOMMF User’s Guide Version 1.0, 1999, Interagency Report NISTIR 6376*. National Institute of Standards and Technology: Gaithersburg, MD.

## ACKNOWLEDGEMENT

DW, AL, SS, and JK have received funding from the European Research Council (ERC) under the Horizon 2020 research and innovation programme of the European Union (grant agreement No 715620). The authors further express their gratitude to M. Lehmann (TU Berlin) for providing access to the FEI Titan 80-300 Holography Special Berlin.

## AUTHOR CONTRIBUTIONS

D.W., S.S., A.L., C.G., B.W. and T.N. performed the experiments. D.W. aligned, reconstructed, and evaluated the 3D data. T.W., N.B. and D.R. fabricated the samples. N.B. carried out the micromagnetic simulations. A.L. and J.K. contributed to the theoretical foundation of VFET and derivation of magnetic properties. D.W., and A.L. wrote the manuscript. N.B. and C.G. contributed to manuscript writing. E.S. and B.B. helped with the interpretation of the data and commented on the manuscript.

## ADDITIONAL INFORMATION

### Competing interests

The authors declare no competing interests.